Synchrotron-Based X-ray Computed Tomography During Compression Loading of Cellular Materials

Nikolaus L. Cordes,[1] Kevin Henderson,[1] Tyler Stannard,[2] Jason J. Williams,[2] Xianghui Xiao,[3] Mathew W. C. Robinson,[4] Tobias A. Schaedler,[5] Nikhilesh Chawla,[2] and Brian M. Patterson[1]*

[1]Polymers and Coatings Group, Materials Science and Technology Division, Los Alamos National Laboratory, P.O. Box 1663, Los Alamos, NM 87545

[2]Department of Materials Science and Engineering, School for Engineering of Matter, Transport, and Energy, Arizona State University, Tempe, AZ 85287-6106

[3]Advanced Photon Source, Argonne National Laboratory, 9700 South Cass Ave., Argonne, IL 60439-4837

[4]Atomic Weapons Establishment, Aldermaston, Reading, Berkshire, RG7 4PR, UK

[5]HRL Laboratories LLC, 3011 Malibu Canyon Rd., Malibu, CA 90265

*bpatterson@lanl.gov

Introduction

Three-dimensional (3D) X-ray computed tomography (CT) of *in situ* dynamic processes provides internal snapshot images as a function of time. Tomograms are mathematically reconstructed from a series of radiographs taken in rapid succession as the specimen is rotated in small angular increments. In addition to spatial resolution, temporal resolution is important. Temporal resolution indicates how close together in time two distinct tomograms can be acquired. Tomograms taken in rapid succession allow detailed analyses of internal processes that cannot be obtained by other means. This article describes the state-of-the-art for such measurements acquired using synchrotron radiation as the X-ray source.

Lab-based CT. Laboratory-based micro-scale X-ray CT, first developed in 1982 by Elliot and Dover [1], is often used to image (in 3D) samples in a static state. With temporal resolutions of ~1 h to 36 h, this technique may be used for the imaging of dynamic processes that occur over long periods of time, similar to time-lapse photography. A recent example of time-lapse CT was published by Lowe et al., in which the authors imaged a living butterfly chrysalis at different stages of metamorphosis [2]. For fast dynamic processes that are not easily controlled, a "post mortem" imaging approach is typically taken, in which X-ray images (that is, tomograms) are acquired before and after the dynamic process [3, 4]. For processes that can be easily controlled, a "quasi-static" (also referred to as "interrupted *in situ*") approach is taken [5, 6]. With this approach, a sample is incrementally exposed to the dynamic process, such as tensile or compressive strains, with tomograms acquired in between each interrupted step; however, some information is lost when the dynamic process is paused (for example, crack propagation) while the tomogram is acquired. Often, either the dynamic process may not be paused, or some information is lost during the pause and therefore the interrupted *in situ* modality is not possible. For example, the interrupted *in situ* compression of soft materials (for example, polymer foams) has been investigated with laboratory-based micro-scale CT, by taking a full tomogram at incremental compression steps [5]. A simple observation of the stress-strain curve (see Figure 7A in reference 5) of a silicone foam shows that stress relaxation of the polymer foam occurs as a result of the applied uniaxial compression. Therefore, in between compression steps, a pause of typically 5 to 15 minutes is needed before the tomogram is acquired. Without this pause, residual motion within the sample leads to blurring of the tomogram and a complete loss of stress relaxation information.

Synchrotron-based CT. For adequate imaging of systems undergoing fast dynamic processes, faster imaging is needed. This requires a high photon flux of the X-ray source, high quantum efficiency of the scintillator (that is, material that converts X-ray photons to visible light photons), and a fast-frame-rate imaging detector. Synchrotron-based X-ray CT, first hypothesized by Grodzins in 1983 [7, 8] and first realized by Thompson et al. in 1984 [9], offers the ideal solution for this problem. Third-generation synchrotron sources [10], such as Argonne National Laboratory's Advanced Photon Source, can offer X-ray photon fluxes ~10^{12} to 10^{14} photons s^{-1}, which is 3 to 5 orders of magnitude brighter than what is available in the laboratory. With the availability of high-speed optical cameras, 4D (the fourth dimension being time) synchrotron-based CT is readily achievable.

Many experiments involving synchrotron-based CT are similar to the lab-based post mortem [11] or interrupted *in situ* [12, 13] experiments. However, recent studies have focused on fast imaging, with temporal resolutions on the order of sub-second to tens of minutes. Recent examples include the investigation of insect mechanics [14, 15], simultaneous heating and continuous compression of an aluminum alloy [16], continuous tensile testing of matrix composites coupled with acoustic emission characterization [17], investigation of creep damage in a brass alloy [18], the solidification of Al-Cu alloys [19], and investigations of fatigue crack growth in SiC particle-reinforced aluminum alloy matrix composites [20].

A current "hot topic" in engineering is additive manufacturing (AM) (also referred to as 3D printing or rapid prototyping), which is the building of 3D structures layer-by-layer with minimal material waste, as opposed to traditional casting or machining methods. For a recent review on the history and current developments of AM, see reference [21]. With AM, unique structures are possible, especially with foams and lattice-structured materials that do not rely on stochastic foaming or pore-templating agents in order to produce voids [22]. Foam structures using AM may be created through direct engineering.

Herein, we describe synchrotron-based CT imaging of two advanced cellular materials undergoing dynamic, continuous

compression (10^{-2} s^{-1} strain rate), with a tomographic temporal resolution of 1 s and spatial resolution of ~15 µm.

Materials and Methods

Foam and microlattice. The first sample described is a 3D printed foam, which was fabricated using an Objet500 Connex 3D printer (Stratasys Ltd., Eden Prairie, MN). The printed material was a rubber-like elastomer (TangoBlack-FullCure 970). This foam exhibits parallel tubular pores in the horizontal direction. The pores exhibit a diameter of 0.75 mm and 1 mm pore spacing.

The second sample is a NiP microlattice. The microlattice was fabricated by self-propogating photopolymer waveguide prototyping, which forms a periodic polymer lattice. The metal microlattice is then fabricated from this template by coating the polymer lattice template using electroless deposition. Etching the polymer template leaves a periodic hollow tube metal microlattice. Details of microlattice fabrication can be found in references [23] and [24].

Tomogram acquisition. Micro-scale X-ray CT was performed at the 2-BM beam line at Argonne National Laboratory's Advanced Photon Source. Details of the tomography setup have been described elsewhere [25, 26]. A polychromatic (pink) beam (centered at ~27 keV) was used. The high photon flux of the pink beam, as compared to a monochromatic white beam, was required for sufficient signal-to-noise in the 1 ms-radiographs. Radiographs were collected using a PCO Dimax high-speed CMOS camera equipped with a 2×Mitutoyo long working distance objective lens, which resulted in 5.8 µm isotropic voxel size in the reconstructed tomograms. Each tomogram consisted of 900 radiographs acquired over 180° sample rotation in 1 s, resulting in a radiograph every 0.2° of sample rotation at ~1 ms intervals. The camera can operate much faster than 900 frames-per-second used here. The rectangular beam geometry produced a field-of-view of 2,016 pixels horizontally (11.09 mm) by 600 pixels vertically (3.30 mm). The memory on the camera was sufficient for ~18,000 radiographs.

Laboratory-based CT operates so that the sample is rotated in discrete angular increments. Rotation motion is halted to allow for radiograph acquisition, typically on the order of seconds to minutes. However, a requirement for tomogram acquisition of fast dynamic processes is that the rotation stage must be synchronized with the radiograph acquisition time. The short 1 ms radiograph acquisition time used in this work required the sample rotation stage to be accelerated to a constant angular velocity during data acquisition in order to be synchronized. Any variation in this velocity would result in a less than ideal tomogram. Ideally, the rotation stage would rotate at a constant angular velocity in one direction for the total duration of the data acquisition (for this study, ~100 s). However, this was not possible due to the location and length of the load

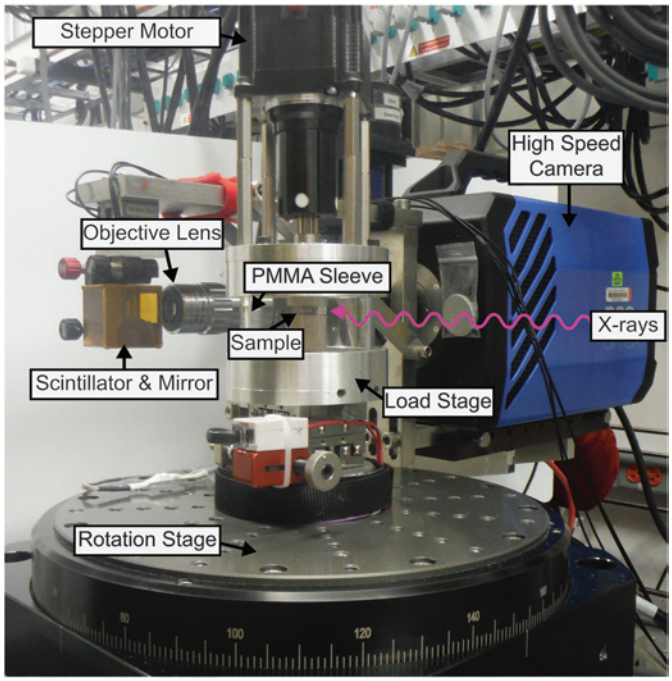

Figure 1: Photo of the loading stage and X-ray CT setup at the APS 2-BM beam line.

stage's power supply cord, which was located at the bottom base of the load stage. Therefore, an oscillating "washing machine" rotation was used. The details of the rotation are as follows: for each tomogram, the sample rotation stage was accelerated clockwise from 0° to 180° in 2 s to a constant angular velocity. The stage was then rotated another 180° clockwise for 1 s at this constant angular velocity, during which 900 radiographs were acquired (constituting the first tomogram). The rotation stage was then decelerated over 180° clockwise for 2 seconds, for a total of 540° rotation per data acquisition cycle. The rotation stage then stopped and reversed direction for the next tomogram, accelerating for 180° anticlockwise, maintaining a constant angular velocity for the next 180° anticlockwise during data acquisition, then decelerating for the next 180°

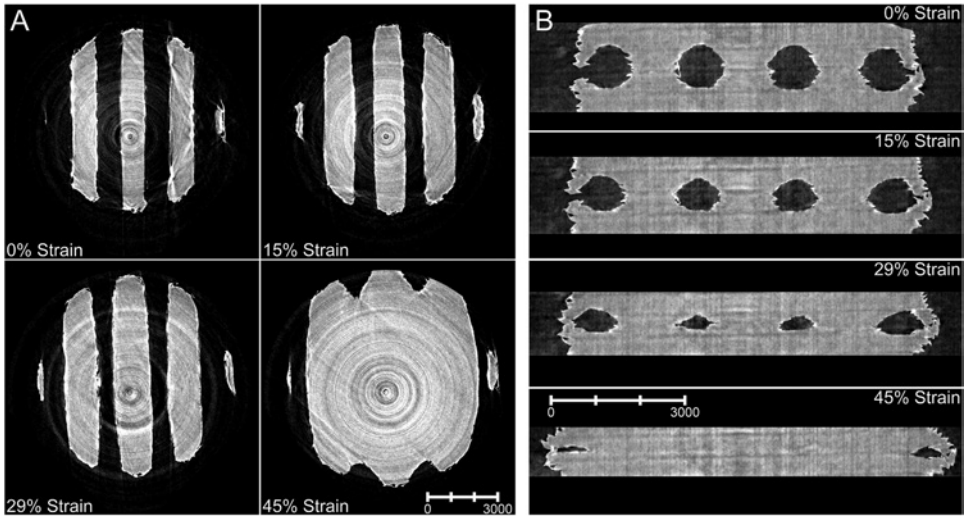

Figure 2: Reconstructed *XY* (A) and *XZ* (B) slices of a 3D printed foam at different stages of compression. The scale bars are in micrometers.

anticlockwise. This procedure was then repeated 18 more times to acquire a total of 20 tomograms per sample.

Tomograms were recorded every fifth second. The compression stage was held stationary during the first tomogram then continuously compressed during the remainder of the tomographic acquisition at a strain rate of $10^{-2}\,s^{-1}$. This procedure was repeated for a total of 20 tomograms, after which a flat-field background and dark-field background, each consisting of 50 radiographs, was acquired. The total duration of the 20-tomogram acquisition took place during a 100 s time span.

Compression tests. The custom loading stage (Figure 1) used for these experiments is described in reference [27]. Compressive loading of the sample was initiated after the first tomogram was acquired, at a strain rate of $10^{-2}\,s^{-1}$. The displacement distance and displacement rate of the loading stage was set to -2.5 mm and 18 µm s^{-1}, respectively, for the 3D printed foam. This resulted in a total compression time of 138.8 s. For the NiP microlattice, the displacement distance and displacement rate was -1 mm and 18 µm s^{-1} respectively, resulting in a total compression time of 55.5 s. Therefore, compression of the NiP microlattice was halted after the 11th tomogram. The drive platen moved approximately three vertical pixels per tomogram and did not lead to image blurring. During compression, samples were not constrained by the X-ray transparent poly(methyl methacrylate) (PMMA) sleeve and were not physically attached to the compression platens. Although total data acquisition time was 100 s, a period of 15–20 minutes was required before the next sample could be imaged, to allow for data transfer from the PCO Dimax camera to the data acquisition PC. Upgrades to the camera controller will increase write and read-out speeds making it possible to increase experimental compression rates by a factor of two.

Data processing. Tomogram reconstruction was performed using TomoPy [28], a Python-based reconstruction program developed at APS. The data were reconstructed and saved as 16-bit slices. Filters used during reconstruction include stripe removal (for example, coif16); phase retrieval (alpha set to 1 or 5×10^{-5} for our samples), which helps to set the best contrast; normalization to maximize the grayscale; and finally a zinger (despeckle) removal [29]. Stripe removal, phase retrieval, and normalization filters are not independent of each other and require several iterations to balance for the best reconstruction. Each data set of 20 tomograms was 96 GB in size.

Reconstructed tomogram visualization and analysis was performed using Avizo Fire version 8.1 (FEI Visualization Sciences Group, Burlington, MA). Smoothing of the reconstructed tomograms of the 3D printed foam was performed using the Edge-Preserving Smoothing filter found in Avizo Fire. No post-reconstruction processing was required for the NiP microlattice tomograms because of the high signal-to-noise ratio of those tomograms. Segmentation of the tomograms was performed using the Interactive Threshold module found in Avizo Fire, resulting in binary images suitable for volume rendering. Post-reconstruction image processing and visualization was performed using a Hewlett-Packard Z820 workstation equipped with 96 GB of RAM, 2 Intel Xeon quad-core processors, and a Nvidia Quadro 6000 graphics card.

Results

3D Printed Foam. Figure 2A presents slices in the *XY* (that is, top-down view) direction of the reconstructed tomograms of the 3D printed foam at 0%, 15%, 29%, and 45% compressive strain. As can be seen in Figures 2A and 2B, four tubular voids are present, which obviously decrease in height and width during uniaxial loading. This decrease is best visualized in the *XZ* (side view) direction presented in Figure 2B. While the two inner tubular voids completely collapse at the last stage of compression (45% strain), there is still void structure present in the two outer tubular voids. This is due to the lack of stress in the lateral direction caused by the limited amount of ligament material in the outer region of the voids. Figure 3 is a stress-strain curve of the 3D printed foam acquired during dynamic uniaxial compression. The curve mostly follows that of a typical elastomeric foam as described by Gibson and Ashby (see Figure 5.1a in reference [30]). The stress-strain curve exhibits a plateau

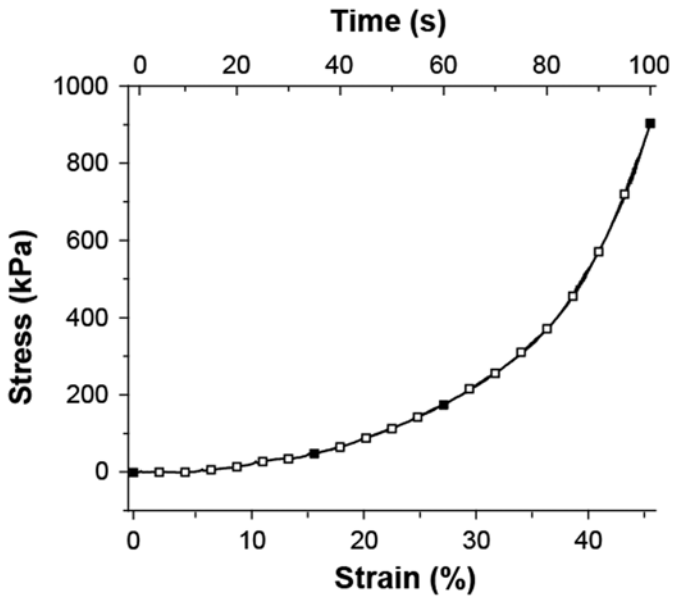

Figure 3: Stress-strain curve of the 3D printed foam acquired during CT imaging. Square symbols indicate times at which a tomogram was acquired. Black squares indicate the tomograms presented in Figures 2 and 4.

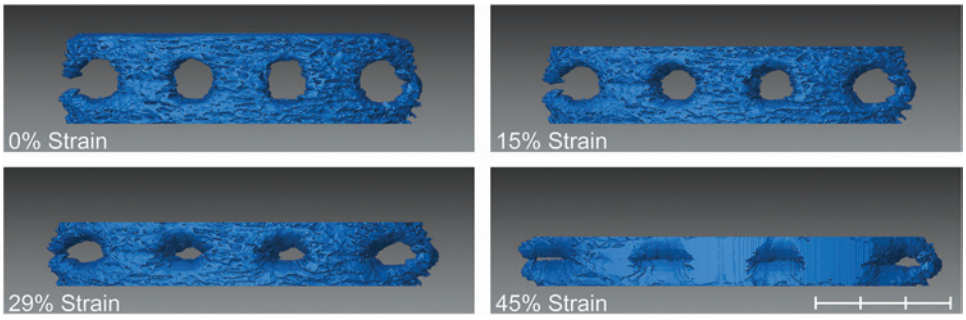

Figure 4: Volume rendering of the 3D printed foam at different stages of compression. The scale bar is 3,000 micrometers.

Figure 5: Top: The same slice as presented in Figure 2A (top left), after applying an edge-preserving smoothing filter. After the smoothing step, the tomogram was segmented (middle) for the foam material. The scale bar is in micrometers. Bottom: The grayscale histograms of the tomograms before and after applying the edge-preserving smoothing filter.

region that begins at 0% compressive strain and extends to ~20% compressive strain, which corresponds to elastic buckling of the foam ligaments. From ~20% compressive strain to 45% compressive strain the stress greatly increases, indicative of densification (which is evident in the volume rendering in Figure 4). Visibly absent from the stress-strain curve is a linear region at low compressive strain, which would correspond to bending of the foam ligaments.

Image noise and ring artifacts in the reconstructed slices (Figure 2) made a direct grayscale-based segmentation of the foam material difficult. Image noise can arise from the performance of the scintillator, the performance of the magnifying optic, and the performance of the detector. Typically, in laboratory-based CT imaging, the acquisition time for a radiograph is increased to sufficiently reduce image noise and increase the number of X-ray photons penetrating the sample per radiograph. This effectively increases the signal-to-noise ratio, resulting in a favorable reconstructed tomogram. With fast dynamic synchrotron-based CT imaging, increasing the acquisition time by even 1 ms would introduce blurring of the sample (at this strain rate), which is considered a less desired image artifact. Ring artifacts in reconstructed tomograms arise from poor detector performance; specifically, a pixel in the detector may have different sensitivity than surrounding pixels during data acquisition, yielding a false grayscale value in the acquired radiographs. If this false grayscale value is present in the majority of radiographs, the reconstructed tomogram will contain a "ring" of higher or lower grayscale value voxels in the *XY* orientation (as seen in Figure 2A). Modern commercially available laboratory-based CT microscopes minimize this type of image artifact by raising and lowering the sample during sample rotation, whereas this would be difficult in fast synchrotron-based CT imaging. To minimize these image artifacts in the reconstruct tomograms, mathematical smoothing filters are often employed (for example, median smoothing filters). For this data set, an edge-preserving smoothing filter was used to smooth the data, which reserves hard edges and smooths or merges soft edges with surrounding features. Figure 5 (top) presents an *XY* (top-down) slice of the foam

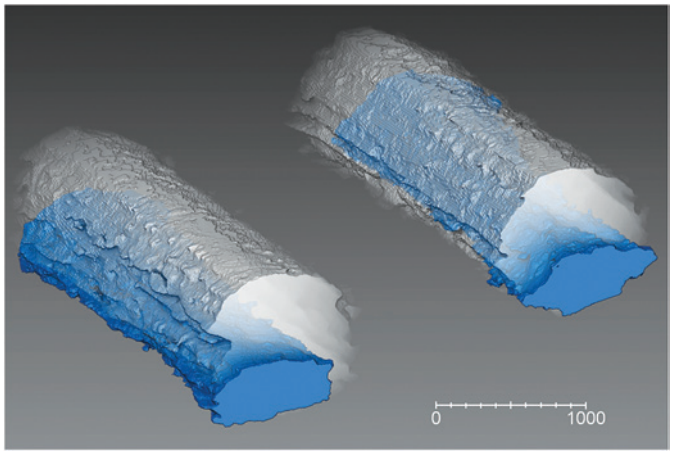

Figure 6: Volume rendering of the two inner voids of the 3D printed foam shown in Figure 2 at 0% compression (white, translucent) and 29% compression (blue, opaque). The scale bar is in micrometers.

Table 1: Physical dimensions of NiP microlattices reported in reference [23] and in this work.

Sample Description		*L* (μm)	*D* (μm)	*t* (μm)	*t*/*D*
Low density[a]	1 mg cm^{-3}	4,000	500	0.12	0.24×10^{-3}
Mid density[b]	14 mg cm^{-3}	1,050	150	0.50	3.33×10^{-3}
High density[c]	43 mg cm^{-3}	1,050	150	1.4	9.33×10^{-3}
Current work[d]	unknown	1,600	260	40	154×10^{-3}

[a]See Figure 3C in reference 23.
[b]See Figure 3A in reference 23.
[b]See Figure 3A in reference 23.
[d]Physical dimensions were measured from CT data.

at 0% compressive strain, after applying an edge-preserving smoothing filter [31] to the data set (compare to Figure 2A, top left). For this data set, the filter performs an adequate smoothing of the noise in three dimensions while keeping desired edges intact, allowing for sufficient grayscale-based segmentation of the tomogram (Figure 5, middle). The histograms of the unprocessed and filtered tomograms (Figure 5, bottom) are radically different, with an increased separation of the two grayscale distributions. By applying this filter to the tomogram, noise is greatly reduced and ring artifacts are virtually eliminated.

From the volume renderings at four stages of compressive strain (Figure 4), the surface roughness of the foam can be visualized. Additionally, the volume rendering allows for a better visualization of the two outer void structures at the 45% compressive strain, when compared to the reconstructed slices presented in Figure 2A. Volume renderings of the two inner tubular voids, at 0% compressive strain and 29% compressive strain, are presented in Figure 6. Segmenting the tomograms for the void structures allows for not only visualization of the void volume, but also quantification of the void height and width as a function of compression.

NiP Microlattice. As stated in the introduction, a NiP microlattice was also imaged during uniaxial loading. This material is similar to those reported by Schaedler et al. [23]. In their report, NiP microlattices exhibited different stress responses during cyclical compressive strains, up to ~50%, which were attributed to different physical dimensions of the lattice. These physical dimensions include *L*, the lattice member length; *D*, the lattice member diameter; and *t*, the lattice member wall thickness (Table 1). NiP microlattices with a small wall thickness-to-diameter ratio (*t*/*D*) exhibited reversible compressive behavior and excellent recovery of their initial shape and height, whereas those with a large *t*/*D* ratio exhibited deformations typical of metallic cellular structures. For the sample examined in this work, the *t*/*D* ratio is much larger (by 2 to 3 orders of magnitude) than those that exhibit reversible compressive behavior (Table 1) because the large wall thickness was 40 μm. This resulted in a loss in plastic deformation, moving directly to brittle fracture of the microlattice, evident in the volume renderings presented in Figure 7, where a broken lattice ligament can be seen lying on the bottom of the loading stage (bottom two images of Figure 7). The stress-time curve of the NiP microlattice sample (Figure 8) exhibits high stress (~1300 kPa) at a time of 25 s, corresponding to the sixth tomogram acquired (Figure 7, top right).

Figure 9 presents a series of radiographs, acquired at different time intervals of the dynamic compression of a separate NiP microlattice sample. These radiographs, acquired during the 6th tomogram of the series, highlight the brittle fracturing of the NiP microlattice during compression. The radiograph acquired at 7 ms (top right) exhibits significant motion blur of the NiP ligaments, due to mechanical failure of the microlattice at the ligament nodes. This failure occurs at a shorter time scale than the radiograph acquisition time, causing the blurring of the image. Also, the direction of the ligaments' movement is perpendicular to the camera. At 396 ms, the sample has rotated 70° from the previous image, thus giving the appearance that ligament bending has not occurred, when in fact the bent ligaments are now parallel to the camera. The black arrow in this radiograph indicates a ligament that broke off of the main body of the sample at two nodes, as can be seen in the 398 ms radiograph (only 2 ms later). In the next four radiographs, the ligament

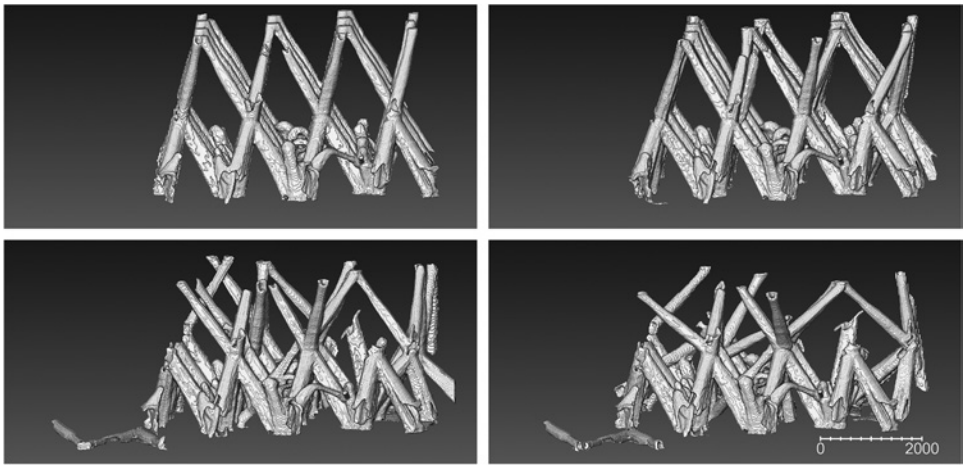

Figure 7: Volume renderings of the NiP microlattice at different periods of compression. The volume renderings correspond to the 1st tomogram (top left), the 6th tomogram (top right), the 8th tomogram (bottom left), and the 13th tomogram (bottom right). The scale bar is in micrometers.

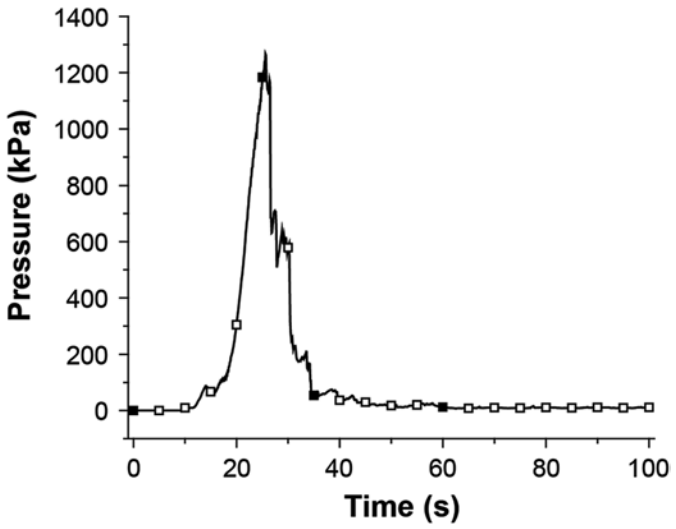

Figure 8: Stress exerted by the NiP microlattice as a function of time, acquired at the same time as the tomograms. Square symbols indicate times at which a tomogram was acquired. Black squares indicate the tomograms presented in Figure 7.

falls toward the bottom of the loading stage at a calculated velocity of 2.3 km h^{-1} (1.4 mph). It should be noted that this particular ligament is absent in the reconstructed tomogram (not shown). This is due to the fact that the ligament is not imaged in a stationary position in each acquired radiograph that is used to reconstruct the tomogram, thus highlighting the fact that the total acquisition time for a tomogram must be significantly shorter than the desired dynamic process that is to be examined.

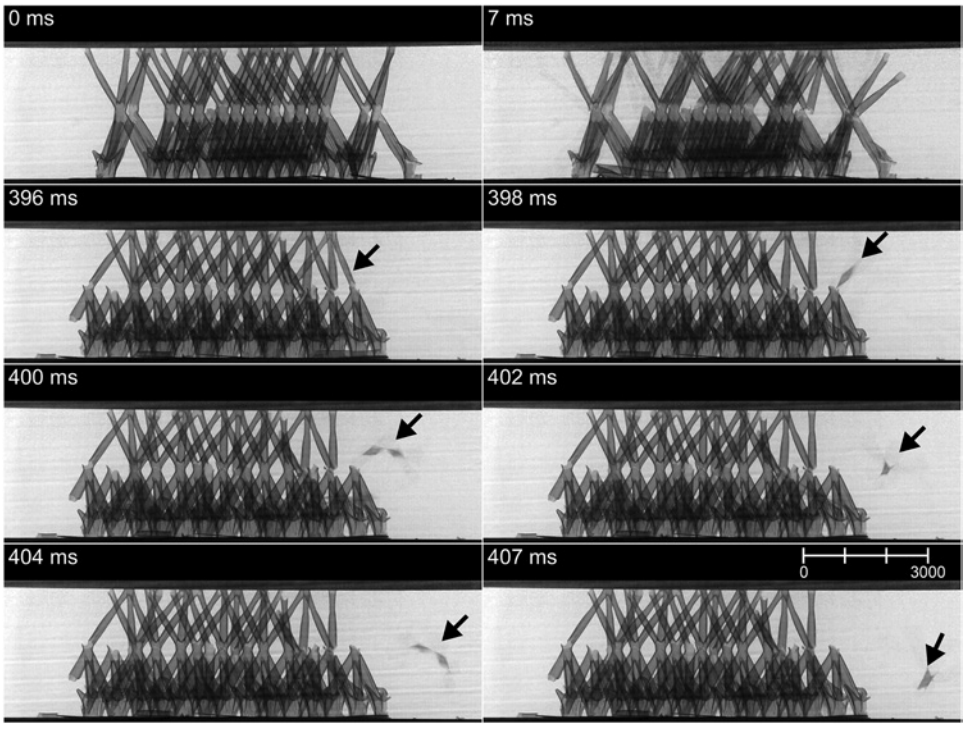

Figure 9: A series of radiographs of a NiP microlattice acquired during dynamic compression. The radiographs show the microlattice at different time intervals (and, consequently, at different rotation angles). The black arrow indicates a ligament that breaks off of the main body of the sample and falls to the bottom of the loading stage. The scale bar is in micrometers.

Discussion

We have demonstrated that coupling a custom loading stage to a third-generation synchrotron-based micro-scale X-ray CT beam line can result in true *in situ* 3D imaging of advanced cellular structures during $10^{-2}\,s^{-1}$ uniaxial compression. The compression rate was chosen so that potential blurring of the acquired tomograms was eliminated. Adequate temporal resolution dictated the spatial resolution of the CT setup. No X-ray radiation-induced damage from the high flux synchrotron X-ray source was noted on either of these samples. However, other samples (such as silicone foams) did have a noticeable yellow discoloration, indicating radiation-induced damage. Also, the PMMA sleeve used to support the upper motor did yellow in the area where the beam passed through and was replaced. Over the following weeks, it shattered within the beam path area. The largest problem with this type of data acquisition is in data handling and analysis. Large volumes of data were acquired for each sample imaged; reconstruction of a single tomogram resulted in a 4.8 GB file size, with a total of 96 GB per sample compression. Therefore, data reconstruction and data processing requires significant amounts of PC processing time and significantly depends on the hardware specifications of the processing PC. For example, the tomograms of the 3D printed foam required an edge-preserving smoothing step [31], which consumed approximately five times the memory of the tomogram data set and took ~16 h to complete with our current processor.

Conclusions

The high photon flux of third-generation synchrotron sources, combined with the high-speed frame rate of commercially available camera systems, have allowed for true 4D micro-scale X-ray CT. Dynamic processes that occur on timescales within a second to tens of minutes can be adequately resolved, with an image resolution of tens of micrometers. This all depends on the sample composition, scintillator performance, synchrotron source photon flux, and frame rate of the image acquisition camera. These data are then suitable for comparison to modeling efforts, using the first tomogram as an initial input and comparing the incremental tomograms to analogous modeled data sets.

Acknowledgements

Los Alamos National Laboratory is operated by Los Alamos National Security LLC under contract number DE-AC52-06NA25396 for the US Department of Energy. Funding for this research was provided by the Enhanced Surveillance Campaign, Tom Zocco, Program Manager. The authors wish to thank Doga Gursoy with his advice in using Tomopy. This research used resources of the

Advanced Photon Source, a U. S. Department of Energy (DOE) Office of Science User Facility operated for the DOE Office of Science by Argonne National Laboratory under Contract No. DE-AC02-06CH11357.

References

[1] JC Elliott and SD Dover, *J Microsc* 126(2) (1982) 211–13.
[2] T Lowe et al., *J R Soc Interface* 10: 20130304(84) (2013) 1–6.
[3] GT Gray III et al., *J Phys: Conf Ser* 500(11) (2014) 112031.
[4] V Yufit et al., *Electrochem Commun* 13(6) (2011) 608–10.
[5] B Patterson et al., *J Mater Sci* 48(5) (2013) 1986–96.
[6] E Padilla et al., *Acta Mater* 60(9) (2012) 4017–26.
[7] L Grodzins, *Nucl Instrum Methods Phys Res* 206(3) (1983) 541–45.
[8] L Grodzins, *Nucl Instrum Methods Phys Res* 206(3) (1983) 547–52.
[9] AC Thompson et al., *Nucl Instrum Methods Phys Res* 222(1–2) (1984) 319–23.
[10] DH Bilderback et al., *J Phys B: At, Mol Opt Phys* 38(9) (2005) S773.
[11] L Babout et al., *Nucl Instrum Methods Phys Res* Sect B 200 (2003) 303–07.
[12] P Bari et al., *Mech Mater* 54 (2012) 84–90.
[13] O Caty et al., *Nucl Instrum Methods Phys Res*, Sect B 324(0) (2014) 113–17.
[14] SM Walker et al., *PLoS Biol* 12(3) (2014) e1001823.
[15] T dos Santos Rolo et al., *Proc Natl Acad Sci USA* 111(11) (2014) 3921–26.
[16] JY Buffière et al., *Exp Mech* 50(3) (2010) 289–305.
[17] E Maire et al., *Acta Mater* 55(20) (2007) 6806–15.
[18] A Pyzalla et al., *Science* 308(5718) (2005) 92–95.
[19] AJ Clarke et al., *Emerging Mater Res* 2(2) (2013) 90–98.
[20] P Hruby et al., *Int J Fatigue* 68(0) (2014) 136–43.
[21] BC Gross et al., *Anal Chem* 86(7) (2014) 3240–53.
[22] BG Compton and JA Lewis, *Adv Mater* 26(34) 2014) 5930–35.
[23] TA Schaedler et al., *Science* 334(6058) (2011) 962–65.
[24] A Torrents et al., *Acta Mater* 60(8) (2012) 3511–23.
[25] F De Carlo et al., *Proc SPIE* 4503 (2002) 1–13.
[26] F De Carlo and B Tieman, *Proc SPIE* 5535 (2004) 644–51.
[27] S Singh et al., *Integr Mater Manuf Innovation* 3(1) (2014) 9.
[28] D Gursoy et al., *J Synchrotron Rad* 21(5) (2014) 1188–93.
[29] Mathworks. "Wavelet families and family members," http://www.mathworks.com/help/wavelet/ref/waveletfamilies.html, 12/10/2014.
[30] LJ Gibson and MF Ashby, *Cellular Solids: Structures and Properties*, 2nd ed., The Press Syndicate of the University of Cambridge, New York, 1997.
[31] J Weickert et al., *IEEE Transactions* 7(3) (1998) 398–410.

MT

https://doi.org/10.1017/S1551929515000190 Published online by Cambridge University Press

LUMENCOR
CUSTOMER FOCUS

Mark Sanders
UNIVERSITY OF MINNESOTA

RELIABILITY and PERFORMANCE

What is the University Imaging Centers network and what is your position in it?

The University Imaging Centers (UIC) is a network of core facility locations for advanced optical imaging and basic electron microscopy located on the University of Minnesota Twin Cities Campus. I am the UIC Program Director.

Reliable performance of your microscopy instrumentation must be a critical factor in the successful operation of University Imaging Centers?

There are several factors that keep me up at night running a facility like ours.

"Firstly, our equipment has to work to specification 100% of the time, in the face of constant demand. Secondly, because we are a chargeback facility, doing everything possible to keep costs low and performance optimal is critical."

There is also a growing requirement to do longer-term (hours to days) live cell imaging. Minimizing the negative impacts of live cell photosensitivity is critical to our facility users.

How have Lumencor's light engines helped University Imaging Centers to meet these demands?

The capacity to electronically select specific wavelength bands from a broad output spectrum source minimizes sample exposure to non-optimal, hazardous wavelengths. Electronic control also allows pulsed excitation, minimizing cell exposure to excitation light and slowing the rate of photobleaching. **Finally, extremely long life cycles of the hardware minimize downtime and configuration/alignment issues.**

www.lumencor.com

https://doi.org/10.1017/S1551929514001917 Published online by Cambridge University Press